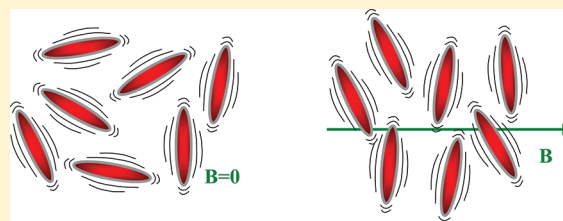


Differential Dynamic Microscopy for Anisotropic Colloidal Dynamics

Mathias Reufer,^{*,†} Vincent A. Martinez,[†] Peter Schurtenberger,[‡] and Wilson C. K. Poon[†][†]SUPA and School of Physics Astronomy, The University of Edinburgh, Edinburgh, United Kingdom[‡]Division of Physical Chemistry, Lund University, Lund, Sweden

ABSTRACT: Differential dynamic microscopy (DDM) is a low-cost, high-throughput technique recently developed for characterizing the isotropic diffusion of spherical colloids using white-light optical microscopy.¹ We develop the theory for applying DDM to probe the dynamics of *anisotropic* colloidal samples such as various ordered phases, or particles interacting with an external field. The q -dependent dynamics can be measured in any direction in the image plane. We demonstrate the method on a dilute aqueous dispersion of anisotropic magnetic particles (hematite) aligned in a magnetic field. The measured diffusion coefficients parallel and perpendicular to the field direction are in good agreement with theoretical values. We show how these measurements allow us to extract the orientational order parameter S_2 of the system.



■ INTRODUCTION

Anisotropic dynamics on the colloidal length scale is ubiquitous in living cells, e.g., because of the local alignment of anisotropic biomacromolecules such as actin filaments or chromosomal DNA. Anisotropic dynamics are also observed in ordered colloidal phases (crystalline or liquid crystalline), and in suspensions where the particles interact with external fields, e.g., sedimentation under gravity or shear.² In particular, external fields can be used to “tune” the single-particle properties as well as the interparticle interaction. Thus, for example, applying electric or magnetic fields induces dipole interactions between the colloids, and gives rise to rich phase diagrams.^{3–6}

A number of experimental techniques are available for the characterization of isotropic colloidal dynamics. In particular, theories for various forms of dynamic light scattering (DLS), including two-color and three-dimensional versions applicable to turbid samples, are well developed. In contrast, the measurement of anisotropic dynamics is notoriously much more challenging. The alignment of the scattering vector q , stray light, and heterodyning due to scattering at the sample–cell interfaces⁴ make DLS on anisotropic samples experimentally extremely demanding. Alternatives are either experimentally sophisticated (heterodyne DLS or laser Doppler spectroscopy),^{7,8} applicable only for large particles (tracking)⁹ or for particles with high X-ray contrast and not affected by beam damage (X-ray photon correlation spectroscopy),¹⁰ or require staining of the system (FRAP: fluorescence recovery after photobleaching).¹¹

We present a simple, reliable, and low-cost technique for characterizing the anisotropic dynamics of a colloidal sample using white-light optical microscopy over a wide range of wave vectors q (in DLS, also termed scattering vector) along any direction in the imaging plane of the sample volume. This technique is a generalization of differential dynamic microscopy (DDM), introduced by Cerbino and Trappe¹ to measure the isotropic diffusion coefficient of spherical colloids, and more

recently applied by Wilson et al.¹² to study the motility of bacteria. In DDM, a time series of digital video images is acquired in bright-field or phase-contrast mode with a fast camera fitted to an ordinary research microscope. The averaged power spectrum of the difference images is then used to calculate the intermediate scattering function (ISF), which describes the dynamics of the system. DDM thus accesses the same dynamical quantity as DLS but, in contrast to DLS, can also be applied to absorbing samples and is less affected by multiple scattering. Moreover, since the method is microscope-based, the user can choose to probe the dynamics of specific spatial regions, a feature that is of particular interest for complex biological samples.

We validate the generalized technique on a dilute aqueous dispersion of anisotropic magnetic particles in bulk aligned in a magnetic field. We use silica-coated spindle-shaped hematite particles with semiaxes $a = 175$ nm and $b = 51.9$ nm, respectively, which align perpendicular to an applied magnetic field.^{13,14} Although their dimensions are well below the optical resolution limit, their dynamics can be accessed by DDM via the intensity fluctuations in the images due to thermal agitation. The optical magnification used for acquiring the images governs the length scale over which we probe the intensity fluctuations and determines the range of the wave vector q of the calculated ISF. We choose $qa < 1$, so that our measured ISF is dominated by translational rather than rotational diffusion.¹⁵ Without applied magnetic field, the particles are randomly orientated, and the measured value for the diffusion coefficient is isotropic (mean over the diffusion coefficients along the three axes of the particle). In case of an applied magnetic field, the particles align with the major particle axis perpendicular to the field and, as a consequence, the measured translational diffusion

Received: December 13, 2011

Revised: February 3, 2012

Published: February 10, 2012



is decreased in the direction parallel to the magnetic field and increased perpendicular to the field compared to the isotropic value. From a measurement of the diffusion along these two directions as a function of magnetic field B , we can extract the orientational order parameter of the system, $S_2(B)$. The latter quantity describes the mean orientation of the particles in the field, and its experimental determination via the dynamics is a novel approach.

THEORY: GENERALIZATION OF DDM FOR ANISOTROPIC DYNAMICS

In this section, we briefly outline the principles of DDM and its extension to apply for samples with asymmetric (e.g., streaming) and anisotropic (e.g., aligned anisotropic particles) dynamics. In DDM, time series of digital video images are acquired in bright-field or phase-contrast mode using a conventional research microscope fitted with a fast camera. Pairs of difference images are then Fourier analyzed as a function of the time delay, τ , between them, with the discretization of the Fourier wave vector q controlled by the frame size. The average square of these Fourier-transformed difference images, or, equivalently, their power spectrum, $g(q, \tau)$, is directly related to the ISF $f(q, \tau)$, which describes the dynamics of the system. The first theoretical derivations of DDM^{1,12} relied on scattering theory to yield the key expression

$$g(q, \tau) = \tilde{A}(q)[1 - f(q, \tau)] + \tilde{B}(q) \quad (1)$$

where $\tilde{A}(q)$ is related to the transfer function of the optical image system and the sample structure imaged, and $\tilde{B}(q)$ is related to the camera noise. In the original experiments¹ demonstrating this methodology, the sample consisted of nearly monodisperse spherical colloidal particles, so that the appropriate expression for the ISF is $f(q, \tau) = \exp(-q^2 D_0 \tau)$, where D_0 is the particles' diffusion coefficient. With this expression for the ISF, eq 1 can be used to fit experimental data to obtain D_0 . Subsequently, an alternative derivation of eq 1 was reported and applied to study the motility of bacteria.¹²

Note that the Fourier space variable appearing in eq 1 is not the wave vector \mathbf{q} , but its magnitude, q , because the derivation leading to this result involves averaging over spatial directions in the imaging plane. Such averaging is appropriate provided that the dynamics are symmetric and isotropic with respect to any direction in the imaging plane. However, for asymmetric dynamics along any direction in the imaging plane, the ISF contains an imaginary part. Moreover, eq 1 does not account for anisotropy, i.e., different dynamics along the different directions in the imaging plane.

Here we give an alternative derivation of DDM. Our derivation has two advantages compared to previous works. First, it is more intuitive, and so makes clear the basic physics of the methodology. Second, it does not average over directions in the image plane, and so gives a generalization of eq 1 that can be applied to asymmetric and anisotropic dynamics.

The raw data in DDM are time-lapsed images $I(\mathbf{r}, t)$, where $\mathbf{r} = (x, y)$ refers to a position in the image plane. Figure 1a shows a generic intensity profile along x with an object whose x -coordinate is x^0 . The term object refers to either a single particle or a locally increased particle concentration (intensity fluctuation) in the case of particles with dimensions below the optical resolution limit. The background intensity I_0 stems from transmitted light that is unaffected by the object. Let the function $A(\mathbf{r})$ represent the object in the image centered at the

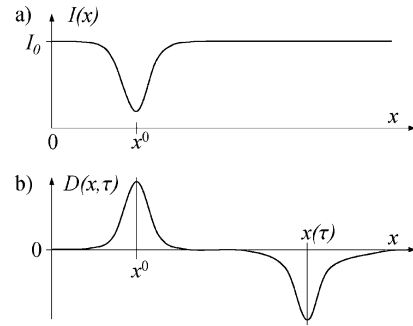


Figure 1. (a) Example of an intensity profile from an object imaged in bright-field or phase contrast mode. (b) Differential signal from an object that moves from $\mathbf{r}^0 = (x^0, 0)$ to $\mathbf{r}(\tau) = (x(\tau), 0)$ in the time τ .

origin, $\mathbf{r} = (0, 0)$, defined such that the intensity pattern of this object is given by $I(\mathbf{r}, t) = I_0 - A(\mathbf{r}, t)$, where $A(\mathbf{r}) \rightarrow 0$ as $|\mathbf{r}| \rightarrow \infty$.

Now consider N identical objects with initial positions $\mathbf{r}_1^0, \mathbf{r}_2^0, \dots, \mathbf{r}_N^0$. Assuming no interference effects (incoherent light), this leads to an initial intensity pattern $I(\mathbf{r}, t = 0) = I_0 - \sum_j^N A(\mathbf{r} - \mathbf{r}_j^0)$. During the time τ , the j th object moves from its initial position \mathbf{r}_j^0 to $\mathbf{r}_j(\tau)$. We define the differential signal $D(\mathbf{r}, \tau) = I(\mathbf{r}, t = \tau) - I(\mathbf{r}, t = 0)$, which can be expressed as

$$D(\mathbf{r}, \tau) = \sum_j^N [A(\mathbf{r} - \mathbf{r}_j^0) - A(\mathbf{r} - \mathbf{r}_j(\tau))] \quad (2)$$

Figure 1b shows the differential signal in the case of the single object ($N = 1$) shown in Figure 1a. Using the shift theorem, we can write the Fourier transform of $D(\mathbf{r}, \tau)$ as

$$F_D(\mathbf{q}, \tau) = A(\mathbf{q}) \sum_j^N [e^{-i\mathbf{q} \cdot \mathbf{r}_j^0} - e^{-i\mathbf{q} \cdot \mathbf{r}_j(\tau)}] \quad (3)$$

where $A(\mathbf{q})$ is the Fourier transform of $A(\mathbf{r})$. The Fourier transform replaces the locations of the objects \mathbf{r} by the wave vector \mathbf{q} and thus introduces the characteristic length scale $1/q$ and the direction \mathbf{q}/q over which motions of the objects occur. We calculate the averaged power spectrum $g(\mathbf{q}, \tau) = \langle |F_D(\mathbf{q}, \tau)|^2 \rangle$ where $\langle \dots \rangle$ stands for the average over M sets of $\{\mathbf{r}_1^0, \dots, \mathbf{r}_N^0, \mathbf{r}_1(\tau), \dots, \mathbf{r}_N(\tau)\}$ with different initial times. In an ergodic system, which can explore all possible configurations in phase space, this time average corresponds to the ensemble average. We introduce the dynamic structure factor $S(\mathbf{q}, \tau) = (1/N) \langle \sum_{j,k}^N e^{-i\mathbf{q} \cdot (\mathbf{r}_j(\tau) - \mathbf{r}_k^0)} \rangle$ and the static structure factor $S(\mathbf{q}) = S(\mathbf{q}, \tau = 0)$. In a stationary system, at a given time τ , each set of positions $\{\mathbf{r}_1(\tau), \dots, \mathbf{r}_N(\tau)\}$ yields the same static structure factor, thus $S(\mathbf{q}) = (1/N) \langle \sum_{j,k}^N e^{-i\mathbf{q} \cdot (\mathbf{r}_j(\tau) - \mathbf{r}_k(\tau))} \rangle = (1/N) \langle \sum_{j,k}^N e^{-i\mathbf{q} \cdot (\mathbf{r}_j^0 - \mathbf{r}_k^0)} \rangle$, and we obtain

$$\begin{aligned} g(\mathbf{q}, \tau) &= |A(\mathbf{q})|^2 \left\langle \sum_{j,k}^N [e^{-i\mathbf{q} \cdot (\mathbf{r}_j^0 - \mathbf{r}_k^0)} - e^{-i\mathbf{q} \cdot (\mathbf{r}_j^0 - \mathbf{r}_k(\tau))} \right. \\ &\quad \left. - e^{-i\mathbf{q} \cdot (\mathbf{r}_j(\tau) - \mathbf{r}_k^0)} + e^{-i\mathbf{q} \cdot (\mathbf{r}_j(\tau) - \mathbf{r}_k(\tau))}] \right\rangle \\ &= N |A(\mathbf{q})|^2 (S(\mathbf{q}) - S^*(\mathbf{q}, \tau) - S(\mathbf{q}, \tau) + S(\mathbf{q})) \end{aligned} \quad (4)$$

Now we link this to the ISF, also known as the normalized dynamic structure factor $f(\mathbf{q}, \tau) = S(\mathbf{q}, \tau)/S(\mathbf{q})$:

$$g(\mathbf{q}, \tau) = 2N|A(\mathbf{q})|^2 S(\mathbf{q}) [1 - \text{Re}(f(\mathbf{q}, \tau))] + \tilde{\mathbf{B}}(q) \quad (5)$$

where $\text{Re}(z)$ stands for the operation of taking the real part of the complex quantity z , and we added $\tilde{\mathbf{B}}(q)$ to take into account (isotropic) noise that stems from the camera.

Interestingly, eq 5 is reminiscent of a result from heterodyne DLS, which deals with unscattered light (local oscillator) mixing with scattered light.¹⁵ From the viewpoint of a near-field scattering experiment, the transmitted (unscattered) light contained in I_0 in DDM might be interpreted as the local oscillator.¹⁶ Importantly, eq 5 shows that DDM can access the dynamics along any direction in real space by choosing \mathbf{q} accordingly. For systems with isotropic dynamics, we can write $q = |\mathbf{q}|$ and $f(\mathbf{q}, \tau) = \text{Re}(f(q, \tau))$, and eq 5 simplifies to eq 1 with $A(q) = 2N|A(q)|^2 S(q)$.

THEORY: DIFFUSION OF ALIGNED ANISOTROPIC PARTICLES

In this section, we provide the theoretical background for the experimental demonstration of the method presented in the last section. As a model system we chose a dilute aqueous dispersion of silica-coated hematite spindle-like particles as shown in Figure 2 that have been characterized before (batch F2 in

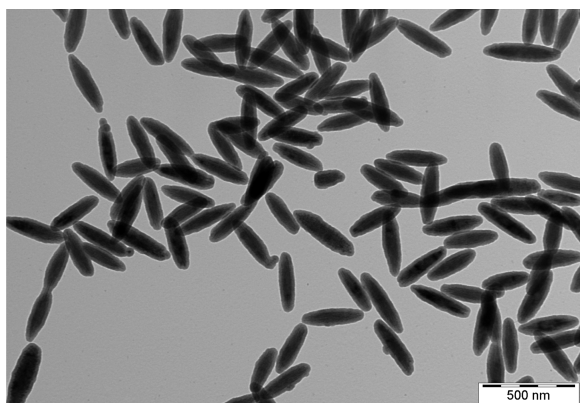


Figure 2. Transmission electron micrograph of synthetic silica-coated spindle-type hematite particles.

ref 13). In this system, we can tune the alignment of the individual particles by using an external homogeneous magnetic field \mathbf{B} . Whereas the field partially suppresses the rotational diffusion, the particles can still undergo unhindered translational diffusion. In our experiments, we select a sufficiently low q -value (i.e., $qa < 1$) such that the measured dynamics are dominated by translational rather than rotational diffusion. The anisotropic shape of the particles leads to different translational Brownian diffusion along their orthogonal axes of symmetry, as illustrated in Figure 3a. However, the dynamics measured on an ensemble of randomly oriented anisotropic particles are isotropic. Only an aligned ensemble of particles leads to an anisotropy in the measured dynamics as depicted in Figure 3b. With our experimental model system, we thus achieve isotropic dynamics at zero field and anisotropic dynamics for oriented particles at high field strength. We characterize the mean alignment of the particles by the second-order orientational order parameter S_2 measured via the degree of anisotropy in the dynamics. The field-dependent $S_2(B)$ describes the transition from isotropic to

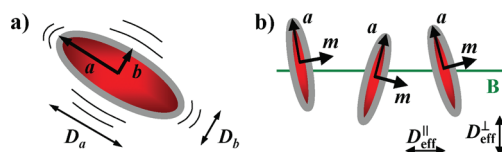


Figure 3. (a) A single silica-coated spindle-type hematite particle with definition of semiaxes and corresponding translational diffusion coefficients. (b) Ensemble of partially aligned particles with definition of effective diffusion coefficients parallel and perpendicular to the applied magnetic field \mathbf{B} .

anisotropic dynamics with increasing field strength B and permits a direct comparison with data obtained by an inherently different technique (i.e., fitting static X-ray scattering patterns¹³).

It has been shown¹⁷ that the hydrodynamic behavior of these silica-coated spindle-type hematite particles can be approximated by a prolate ellipsoid with major semiaxis a and minor semiaxis b . The isotropic translational diffusion coefficient of a prolate ellipsoid is calculated as the average over the diffusion coefficients along the different axes¹⁵

$$D_{\text{iso}} = \frac{1}{3}(D_a + 2D_b) \quad (6)$$

where D_a and D_b are the translational diffusion coefficients of a prolate spheroid parallel to the semiaxes a and b , respectively. Expressions for D_a and D_b for stick boundary conditions were first calculated by Perrin.¹⁸ Note that $D_a/D_b < 2$ for all finite aspect ratios, and $D_a/D_b = 2$ in the limit of infinite long and thin cylindrically symmetric rods.¹⁹

With an applied magnetic field \mathbf{B} , the individual hematite particles align such that their magnetic moments \mathbf{m} are parallel to \mathbf{B} . But the anisotropy in the dynamics are determined by the orientation of the major semiaxis \mathbf{a} . To link the orientation of \mathbf{m} to the particle orientation \mathbf{a} , we need to consider the magnetic properties of hematite. Hematite has a corundum-type crystal structure with space group $R3c$, and is a canted antiferromagnet at room temperature, with a small resulting magnetic moment m in the basal plane.²⁰ The magnetic moment can switch rather easily in the basal plane due to the small magnetic anisotropy energy within the plane compared to the energy required to tilt \mathbf{m} out of the basal plane.²⁰ It has been shown^{13,14} that the synthesized spindle-type hematite particles are monocrystalline with the basal plane perpendicular to the major particle semiaxis \mathbf{a} , thus \mathbf{m} is perpendicular to \mathbf{a} . As a result, in the limit of a very strong magnetic field \mathbf{B} , the particle orientation \mathbf{a} is restricted to the plane perpendicular to \mathbf{B} , but \mathbf{a} is free to rotate around the direction of \mathbf{B} .

Hence, for noninteracting particles, we expect to observe with increasing field an alignment of the individual particles along with a slowing down of the dynamics measured parallel to \mathbf{B} from D_{iso} at zero field to D_b in the limit of high field strength, and perpendicular to \mathbf{B} to increase from D_{iso} at zero field to $(D_a + D_b)/2$. The field-dependent effective diffusion coefficients, measured parallel and perpendicular to \mathbf{B} , are given by²¹

$$\begin{aligned} D_{\text{eff}}^{\parallel}(B) &= D_{\text{iso}} + \frac{2}{3}(D_a - D_b)S_2(B) \xrightarrow{B \rightarrow \infty} D_b \\ D_{\text{eff}}^{\perp}(B) &= D_{\text{iso}} - \frac{1}{3}(D_a - D_b)S_2(B) \xrightarrow{B \rightarrow \infty} \frac{1}{2}(D_a + D_b) \end{aligned} \quad (7)$$

where $S_2(B)$ is the second-order orientational order parameter defined as $S_2(B) = \langle P_2((\mathbf{a} \cdot \mathbf{B})/(aB)) \rangle$, and $P_2(x) = (3x^2 - 1)/2$ is the second Legendre polynomial. For a randomly oriented sample we find $S_2 = 0$, and a fully aligned sample (i.e., \mathbf{a} perpendicular to \mathbf{B}) yields $S_2 = -0.5$.

MATERIAL AND METHODS

We used silica-coated spindle-type hematite particles with mean values for the semiaxes $a = 175 \pm 10$ nm and $b = 51.9 \pm 5$ nm and polydispersity $\sigma^{\text{TEM}} = 0.13$ (defined as standard deviation over mean) from the batch F2 described in ref 13. Those values were determined by statistical analysis of transmission electron microscopy (TEM) images, and the (systematic) errors of ± 10 nm and ± 5 nm are associated with the threshold chosen to fit the contour lines and particles that are not laying with the major semiaxis flat in the image plane. The particles were dispersed in distilled water at a concentration of 0.02 wt % and filled in a customized observation chamber (with thickness of 40 μm along the optical axis) glued with UV-cure adhesive and sealed with Vaseline. A water-cooled electromagnet (Newport Instruments, type C) was attached to an inverted research microscope (Nikon TE300 Eclipse) such that the field direction was horizontal. The sample was mounted in the air gap (26 mm) between the two iron cores of the electromagnet. The large size of the iron cores (40 mm diameter) compared to the sample ensures a homogeneous magnetic field in the field of view. We used phase-contrast mode (Ph2 condenser, Nikon Plan Fluor 60 \times objective with numerical aperture = 0.7) and collected images from the bulk of the sample chamber (away from the walls to avoid wall effects) with a CMOS camera (Mikrotron MC 1362) and frame grabber card (Mikrotron Inspecta 5). Although the electromagnet was water-cooled, the temperature in the sample environment rose from initially 22.6 $^\circ\text{C}$ (room temperature) to approximately 23.1 $^\circ\text{C}$ during the measurements. We therefore recorded during the experiments every 6 min an image sequence at zero field and normalized the subsequent data to the initial particle dynamics. The corrections applied were $\leq 1.8\%$. The effective inverse pixel size $k = 4.33$ pixel/ μm , accounting for the magnification of the microscope, was found by imaging a calibration slide with 10 μm scale and measuring the resulting pixel distance with an image processing program (ImageJ). The camera was rotated by 45 $^\circ$ such that the applied magnetic field was diagonal on the image (see Figure 4). This configuration reduces the impact of the

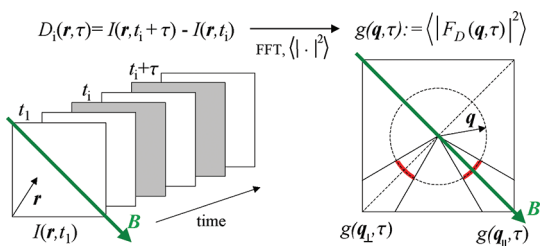


Figure 4. Schematic of the data processing procedure. The azimuthal averaging is done along the arc length (red) of $\pm 15^\circ$ parallel and perpendicular to the direction of the magnetic field \mathbf{B} to obtain $g(\mathbf{q}_{\parallel}, \tau)$ and $g(\mathbf{q}_{\perp}, \tau)$, respectively.

artifacts stemming from the Fourier transform of the finite images, which appear mainly along the horizontal and vertical directions.²²

Figure 4 illustrates the data processing to obtain $g(\mathbf{q}, \tau)$ from the image sequence (3740 images with 512×512 pixels at

frame rate 1000 fps) collected in an experiment. For a given delay time τ , the differential images $D_i(\mathbf{r}, \tau) = I(\mathbf{r}, t_i + \tau) - I(\mathbf{r}, t_i)$ are calculated for a set of $M = 666$ different initial times t_i (typically we choose $t_1, t_4, t_8, \dots, t_{1999}$). After performing the fast Fourier transform (FFT) and calculating the square of the absolute value, the $g(\mathbf{q}, \tau)$ for this particular value of τ is computed as the average over the different initial times t_i . To obtain values for $g(\mathbf{q}_{\parallel}, \tau)$ where $\mathbf{q}_{\parallel} \parallel \mathbf{B}$, and $g(\mathbf{q}_{\perp}, \tau)$ where $\mathbf{q}_{\perp} \perp \mathbf{B}$, we calculate the azimuthal average in the \mathbf{q} -plane of $g(\mathbf{q}, \tau)$ for the sectors of $\pm 15^\circ$ parallel and perpendicular to \mathbf{B} . We use linear interpolation between the four adjacent points in the discrete \mathbf{q} -space along an arc length defined by points with angular spacing of 1° and radius q . The choice of the sector size is a compromise between good statistics (large sector size) and low contribution from the perpendicular dynamics (small sector size). The choice of $\pm 15^\circ$ yields sufficient statistics and the contribution of the perpendicular dynamics was calculated to be 3.4% only, which is negligible since the measured $D_{\text{eff}}^{\parallel}$ and D_{eff}^{\perp} differ by 10% at the most. The above procedure is repeated for a set of 112 different delay times τ (logarithmically spaced in time) to obtain the full time dependency of $g(\mathbf{q}_{\parallel}, \tau)$ and $g(\mathbf{q}_{\perp}, \tau)$.

DLS was performed at a temperature of 22.5 $^\circ\text{C}$ on a ALV/CGS-3 goniometer system with ALV/LSE-5004 multiple τ correlator and HeNe-Laser (22 mW, $\lambda_0 = 632.8$ nm). The decay rate $\Gamma = q^2 D_{\text{iso}}^{\text{DLS}}$ was determined by a second-order cumulant fit of the intensity correlation function measured at scattering angles in the range from 13 $^\circ$ to 26 $^\circ$ ($q = 3.0$ – 6.0 μm^{-1}). The isotropic translational diffusion coefficient $D_{\text{iso}}^{\text{DLS}} = 2.15 \pm 0.08$ $\mu\text{m}^2/\text{s}$ was found by a linear fit of $\Gamma(q^2)$.

RESULTS AND DISCUSSION

In this section we present the experimental demonstration of the generalization of DDM. To investigate the field-dependent dynamics of the system, we collect image sequences for different applied field strengths B and process the data to obtain the corresponding $g(\mathbf{q}_{\parallel}, \tau)$ and $g(\mathbf{q}_{\perp}, \tau)$. Figure 5

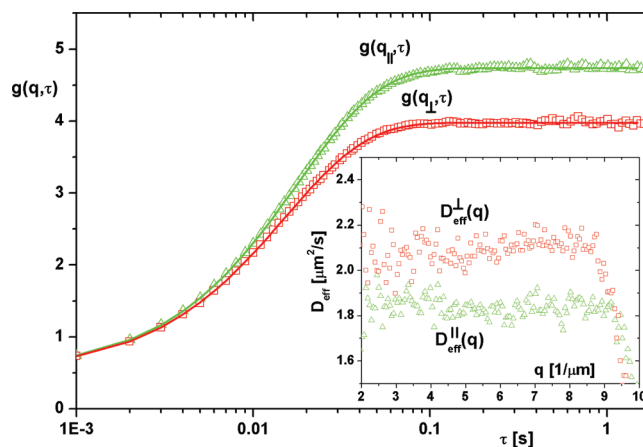


Figure 5. Measured $g(\mathbf{q}, \tau)$ at $q = 5.56$ μm^{-1} along (green triangles) and perpendicular to (red squares) a field of $B = 430$ mT. The fits (lines) allow to extract values for the q -dependent effective diffusion coefficients (inset) from which $D_{\text{eff}}^{\parallel}$ and D_{eff}^{\perp} are calculated as the average over the restricted q -range.

shows representative data at $q = 5.56$ μm^{-1} for an applied magnetic field of $B = 430$ mT. A fit of the data reveals the anisotropic dynamics. We use eq 5 and the cumulant expansion

$f(q, \tau) \approx \exp(-\Gamma\tau)(1 + \sigma\Gamma^2\tau^2/2)$ with $\Gamma = q^2 D_{\text{eff}}$ as a fit function with $\tilde{A}(q)$, $\tilde{B}(q)$, D_{eff} and σ as fitting parameters. The fit yields a moderate polydispersity of $\sigma \approx 0.10$ in good agreement with the value determined by the statistical analysis of TEM images ($\sigma^{\text{TEM}} = 0.13$).

The inset of Figure 5 shows the obtained q -dependent values for the effective diffusion coefficients $D_{\text{eff}}^{\parallel}(q)$ and $D_{\text{eff}}^{\perp}(q)$ for an applied magnetic field of $B = 430$ mT. For further processing, we restrict the data collection to the q -range from 3.0 to 8.0 μm^{-1} because, at lower q -values, the total length of the image sequences are too short (3740 images) to reveal the noise floor, which results in poorer statistics, whereas at higher q -values the chosen frame rate (1000 fps) is not sufficient to capture the initial rise in $g(q, \tau)$. Thus, the number of images in the sequence and the chosen frame rate define the accessible q -range. For each field strength, $D_{\text{eff}}^{\parallel}$ and D_{eff}^{\perp} are calculated as the mean in the restricted q -range, and the error bars are twice the standard deviation divided by the square root of the number of values. Figure 6 shows the obtained $D_{\text{eff}}^{\parallel}(B)$ and $D_{\text{eff}}^{\perp}(B)$. With

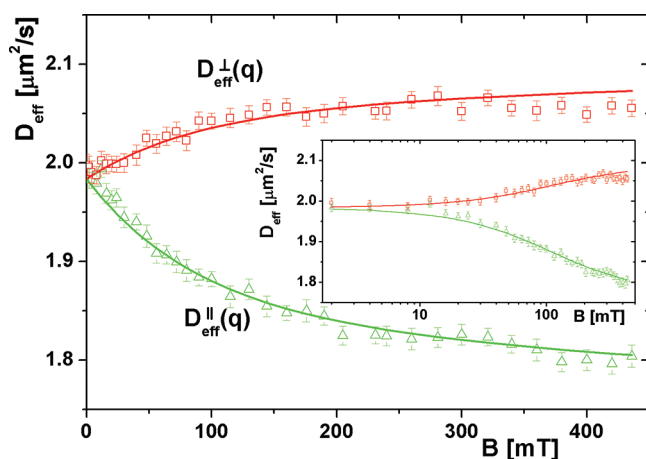


Figure 6. Measured effective diffusion along the field direction (green triangles) $D_{\text{eff}}^{\parallel}(B)$ and perpendicular to the field (red squares) $D_{\text{eff}}^{\perp}(B)$. The lines represent the fit described in the text. The inset shows the same data in semilogarithmic representation.

increasing field, $D_{\text{eff}}^{\parallel}(B)$ and $D_{\text{eff}}^{\perp}(B)$ diverge from each other and saturate at separate values. This reflects the alignment of the individual particles with their major axis perpendicular to the field direction. The zero field value $D_{\text{iso}}^{\text{DDM}} = D_{\text{eff}}(B = 0) = 1.99 \pm 0.02 \mu\text{m}^2/\text{s}$ is in good agreement with the diffusion coefficient measured by DLS $D_{\text{iso}}^{\text{DLS}} = 2.15 \pm 0.08 \mu\text{m}^2/\text{s}$.

In the next step we use eq 7 to extract $S_2(B)$ from the data in Figure 6 and compare it to data from the literature measured on the same batch of particles. The second-order orientational order parameter $S_2(B)$ describes the mean alignment of the particles and therefore the transition from $D_{\text{iso}}^{\text{DDM}}$ at zero field to the separated values at high field strength in Figure 6. However, in order to fit eq 7 to the data, we need an empirical ansatz for $S_2(B)$ with parameters determining the shape of the transition that fulfills the limits of zero and infinite field strengths ($S_2(0) = 0$, $S_2(\infty) = -0.5$). The choice of the ansatz is not critical as long as it fits the data well since we use it only to construct $S_2(B)$. The lines in Figure 6 show the fit with eq 7 and the ansatz $S_2(B) = (e^{-p_1 B} + e^{-p_2 B} - 2)/4$, which yields the best-fit parameters $D_a^{\text{DDM}} = 2.53 \mu\text{m}^2/\text{s}$, $D_b^{\text{DDM}} = 1.71 \mu\text{m}^2/\text{s}$, $p_1 = 0.90 \text{ T}^{-1}$, and $p_2 = 11.3 \text{ T}^{-1}$. Figure 7 compares the $S_2(B)$ reconstructed from this empirical ansatz with data obtained

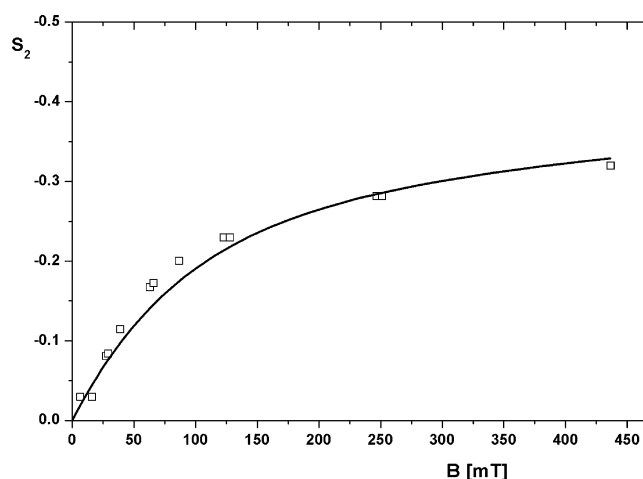


Figure 7. Obtained second-order orientational order parameter $S_2(B)$ (line) compared with data (squares) from ref 13.

by X-ray scattering¹³ from the same batch of particles. The agreement between the two $S_2(B)$ measured with inherently different techniques is very good.

Note that for systems where we reach fully oriented conditions, the extraction of $S_2(B)$ can be simplified, and no empirical ansatz is necessary. In this case, the saturation values for $D_{\text{eff}}^{\parallel}(B)$ and D_{eff}^{\perp} permit the calculation of D_a , D_b , and D_{iso} , which allows the extraction of $S_2(B)$ by using eq 7.

Finally, for systems with well-defined magnetic properties, the analytical expression $S_2(B) = \langle P_2((\mathbf{a} \cdot \mathbf{B})/(aB)) \rangle$ can also be calculated by using the Boltzmann factor $\exp(\mathbf{m} \cdot \mathbf{B}/k_B T)$, where k_B is the Boltzmann constant and T is the temperature.^{13,21} However, the dependency of m on the field (paramagnetic contribution) and the experimental time scale (magnetic relaxation time) in combination with the perpendicular orientation of the magnetic moment m with respect to the major particle axis a complicates this for the chosen system.¹⁴ An analytical calculation of $S_2(B)$ would require several assumptions and is thus not within the scope of this work. However, it is interesting to compare the found onset of orientational order with the potential of the particles in the magnetic field. A particle with magnetic moment m in a magnetic field B experiences a potential energy of the order of mB , whereas the relevant energy that randomizes its orientation is $k_B T$. For similar particles, a magnetic moment $m = 1.4 \times 10^{-19} \text{ J T}^{-1}$ was found at low field strength,¹³ which defines the critical field $B_{\text{crit}} = k_B T/m \approx 30 \text{ mT}$, where the potential energy is equal to the thermal energy. This corresponds well to the observed onset of orientational order, as apparent in the inset of Figure 6.

Finally, we can compare the found values for $D_{\text{iso}}^{\text{DDM}}$, D_a^{DDM} , and D_b^{DDM} to calculations for an ellipsoidal body¹⁸ based on the particle dimensions from the statistical evaluation of TEM images. However, the polydispersity has to be taken into account since the scattering intensity and thus the contrast is proportional to the squared particle mass.¹⁵ We use a weighting of the individual values that is proportional to the particle volume squared¹⁷ and find mean values of $D_{\text{iso}}^{\text{TEM}} = 2.44 \mu\text{m}^2/\text{s}$, $D_a^{\text{TEM}} = 2.82 \mu\text{m}^2/\text{s}$ and $D_b^{\text{TEM}} = 2.24 \mu\text{m}^2/\text{s}$. The measured values for D_{iso} , D_a and D_b are 18%, 10%, and 23%, respectively, lower than the calculated values.

In a recent study on similar particles,¹⁷ measurements of D_{iso} with DLS also revealed lower values (by 2–8%) compared to predictions based on the Perrin theory. However, it was also

pointed out that the calculated D_{iso} might be affected by systematic errors in the measurements of the particle dimensions based on TEM micrographs. In particular, the obtained values for a and b depend on the chosen threshold to find the particle contours and the model for the particle shape (e.g., ellipse) to identify particles on the micrographs. Another possible explanation for the deviations might be the presence of a few small aggregates (which are visible in the image sequences) leading to a small contribution of slow isotropic dynamics that lowers the measured values for D_{eff} . This assumption is supported by the good agreement of the measured values for D_{iso} determined by DDM and DLS.

CONCLUSION

We have generalized the DDM technique to samples with asymmetric and anisotropic dynamics. This generalized DDM represents an effective alternative to traditional methods, which are mostly experimentally challenging. In contrast, DDM requires no specialist apparatus, and is both fast and robust. We used a model system of anisotropic magnetic particles to experimentally validate the generalized technique. The quality of the data obtained demonstrates the robustness of the technique.

Moreover, the theoretical framework developed here is not restricted to simple Brownian dynamics. It permits the application of DDM to various other types of dynamics by employing the appropriate ISF. In particular, the possibility of investigating asymmetric dynamics opens the route to study transport and flow phenomena as encountered in biological samples. It also facilitates the characterization of highly absorbing systems by simplifying the collection of data from samples so thin that absorption is not a problem. In fact, absorption even increases the optical contrast for DDM, leading to a better signal-to-noise ratio. This contrasts strongly with DLS, where absorbed light does not contribute to the measured signal, which only depends on scattered light. Furthermore, the use of white light for the imaging reduces the impact of multiple scattering on the data drastically due to its low spatial coherence. This opens the possibility of characterizing samples with high particle concentrations. As an example, it might allow the investigation of the dynamics of ferrofluids in magnetic fields at concentrations where dipole interactions are important and thus exhibit anisotropic dynamics.

Finally, the presented approach of measuring S_2 via the anisotropic Brownian dynamics is, to our knowledge, novel and can be applied to various dilute systems consisting of particles with anisotropic shape.

AUTHOR INFORMATION

Corresponding Author

*E-mail: mathias.reufer@ed.ac.uk.

Notes

The authors declare no competing financial interest.

ACKNOWLEDGMENTS

We thank Hervé Dietsch for help with particle synthesis, Jochen Arlt for help with initial set up, and Urs Gasser and Ilya Martchenko for stimulating discussions. This work is supported by the Swiss National Science Foundation (PBF2-127867 and 200021_127192), EPSRC (EP/E030173/1 and EP/D071070/1), and FP7-PEOPLE (PIIF-GA-2010-276190).

REFERENCES

- (1) Cerbino, R.; Trappe, V. Differential dynamic microscopy: Probing wave vector dependent dynamics with a microscope. *Phys. Rev. Lett.* **2008**, *100*, 188102.
- (2) Cheng, X.; Xinliang, X.; Rice, S. A.; Dinner, A. R.; Cohen, I. Assembly of vorticity-aligned hard-sphere colloidal strings in a simple shear flow. *Proc. Natl. Acad. Sci. U.S.A.* **2012**, *109*, 63–67.
- (3) Leunissen, M. E.; Christova, C. G.; Hynninen, A. P.; Royall, C. P.; Campbell, A. I.; Imhof, A.; Dijkstra, M.; van Roij, R.; van Blaaderen, A. Ionic colloidal crystals of oppositely charged particles. *Nature* **2005**, *437*, 235. Leunissen, M. E.; Vutukuri, H. R.; van Blaaderen, A. Directing colloidal self-assembly with biaxial electric fields. *Adv. Mater.* **2009**, *21*, 3116–3120.
- (4) Kang, K.; Dhont, J. K. G. Electric-field induced transitions in suspensions of charged colloidal rods. *Soft Matter* **2010**, *6*, 273–286.
- (5) Tang, J.; Fraden, S. Magnetic-field-induced isotropic-nematic phase transition in a colloidal suspension. *Phys. Rev. Lett.* **1993**, *71*, 3509–3512.
- (6) Lemaire, B. J.; Davidson, P.; Ferré, J.; Jamet, J. P.; Petermann, D.; Panine, P.; Dozov, I.; Jolivet, J. P. Physical properties of aqueous suspensions of goethite (α -FeOOH) nanorods. *Eur. Phys. J. E* **2004**, *13*, 291–308.
- (7) Mustacich, R. V.; Ware, B. R. Observation of protoplasmic streaming by laser-light scattering. *Phys. Rev. Lett.* **1974**, *33*, 617–620.
- (8) Yeh, Y.; Cummins, H. Z. Localized fluid flow measurements with an He–Ne Laser spectrometer. *Appl. Phys. Lett.* **1964**, *4*, 176–178.
- (9) Han, Y.; Alsayed, A. M.; Nobili, M.; Zhang, J.; Lubensky, T. C.; Yodh, A. G. Brownian motion of an ellipsoid. *Science* **2006**, *314*, 626–630.
- (10) Wagner, J.; Autenrieth, T.; Robert, A.; Härtl, W.; Grübel, G. Structure and dynamics of complex liquids with magnetic dipole–dipole interactions by means of static and dynamic X-ray scattering. *J. Magn. Magn. Mater.* **2005**, *289*, 54–57.
- (11) van Bruggen, M. P. B.; Lekkerkerker, H. N. W.; Maret, G.; Dhont, J. K. G. Long-time translational self-diffusion in isotropic and nematic dispersions of colloidal rods. *Phys. Rev. E* **1998**, *58*, 7668–7677.
- (12) Wilson, L. G.; Martinez, V. A.; Schwarz-Linek, J.; Tailleur, J.; Bryant, G.; Pusey, P. N.; Poon, W. C. K. Differential dynamic microscopy of bacterial motility. *Phys. Rev. Lett.* **2011**, *106*, 018101.
- (13) Reufer, M.; Dietsch, H.; Gasser, U.; Hirt, A.; Menzel, A.; Schurtenberger, P. Morphology and orientational behavior of silica-coated spindle-type hematite particles in a magnetic field probed by small-angle X-ray scattering. *J. Phys. Chem. B* **2010**, *114*, 4763–4769.
- (14) Reufer, M.; Dietsch, H.; Gasser, U.; Grobety, B.; Hirt, A. M.; Malik, V. K.; Schurtenberger, P. Magnetic properties of silica coated spindle-type hematite particles. *J. Phys.: Condens. Matter* **2011**, *23*, 065102.
- (15) Berne, B. J.; Pecora, R. *Dynamic Light Scattering*; Dover: New York, 2000; pp 40–180.
- (16) Cerbino, R.; Vailati, A. Near-field scattering techniques: Novel instrumentation and results from time and spatially resolved investigations of soft matter systems. *Curr. Opin. Colloid Interface Sci.* **2009**, *14*, 416–425.
- (17) Martchenko, I.; Dietsch, H.; Moitzi, C.; Schurtenberger, P. Hydrodynamic properties of magnetic nanoparticles with tunable shape anisotropy: Prediction and experimental verification. *J. Phys. Chem. B* **2011**, *115*, 14838–14845.
- (18) Perrin, F. Mouvement brownien d'un ellipsoïde (I). Dispersion diélectrique pour des molécules ellipsoïdales. *J. Phys. Radium* **1934**, *7*, 497–511. Perrin, F. Mouvement brownien d'un ellipsoïde (II). Rotation libre et dépolarisation des fluorescences. Translation et diffusion des molécules ellipsoïdales. *J. Phys. Radium* **1936**, *7*, 1–11.
- (19) Brown, W. *Dynamic Light Scattering: The Method and Some Applications*; Clarendon Press: Oxford, 1993; pp 519.
- (20) O'Reilly, W. *Rock and Mineral Magnetism*; Blackie: Glasgow, 1984; pp 172–179.

(21) Ilg, P. Anisotropic diffusion in nematic liquid crystals and in ferrofluids. *Phys. Rev. E* **2005**, *71*, 051407.

(22) Martinez, V. A.; Besseling, R.; Croze, O. A.; Tailleur, J.; Reufer, M.; Schwarz-Linek, J.; Wilson, L. G.; Bees, M. A.; Poon, W. C. K. Differential dynamic microscopy: A high-throughput method for characterizing the motility of microorganisms. *Biophys. J.* Submitted, available from arXiv:1202.1702v1.